

A numerical approach to reconstruct mesoscopic yarn section of textile composites based upon X-ray micro-tomography

Y. LIU^a, D.VASIUKOV^b, S. PANIER^c

- a. Polymers and Composites Technology & Mechanical Engineering Department, IMT Lille Douai, France, yang.liu@imt-lille-douai.fr
- b. Polymers and Composites Technology & Mechanical Engineering Department, IMT Lille Douai, France, dmytro.vasiukov@imt-lille-douai.fr
- c. Laboratoire des Technologies Innovantes, LTI-EA 3899, Université de Picardie Jules Verne, Amiens, France, stephane.panier@u-picardie.fr

Abstract

The efficiency of the mesoscopic models has been proven for prediction of the damage and failure behaviour of textile composites. In classical mesoscopic models, the section of yarn is usually simplified as circular, lenticular, ellipsoidal or more sophisticated shapes defined by a power ellipse. A numeric tool is proposed in this work to reconstruct the yarn section based upon realistic geometry obtained via X-ray micro-tomography techniques. The sectional shape of yarn is fit as a polygon by connecting the selected boundary key points. Improved Lubachevsky-Stillinger algorithm is then employed to drive the motion and growth of the fibre sections within the yarn's domain until the specified fibre volume fraction is reached. The proposed method shows excellent performance on modelling the gradually varied packing of fibres. As an example, the irregular yarn shape has been modelled with varying fibre fraction. This allows analysing the influence of the fibre packing on fibre-matrix debonding and transversal crack localisation. This approach can be used for arbitrary textile composite where the fibre can be taken as a circle at the microscale, as long as the real geometry of yarn is provided by micro-tomography or other experimental observation techniques.

Keywords: Textile composites; X-ray micro-tomography; Shape reconstruction; Micro-modeling; Constitutive modelling.

1 Introduction

3D woven composites have gained a wide range of applications in many industrial domains for their excellent multi-directional load bearing capacity, high delamination resistance, and good impact strength. When to predict the mechanical properties of the 3D composites, numerical simulations were generally employed by taking advantage the computational economy. In a typical numerical model, the assignment of the yarn properties and the yarn geometry play a decisive role on the final predicted mechanical performance of the composite structure.

In most of the currently used mesoscopic models, the yarns are commonly considered as a homogeneous material with the effective properties estimated by analytical formulae, where the elastic constants are expressed as the function of fibre volume fraction and the basic constituents' properties. It is indicated in [1] that the assumption of the homogeneous yarn leads to an underestimation of the stress concentration, due to the fact that the real stress concentration region, which is caused by the densely packed fibres, has been smeared out. In latest research [2], the intra-yarn fibre volume fraction gradients (IY-FVFG) is employed to characterise the inhomogeneity of the fibre packing inside the yarn section. The IY-FVFG is determined by Voronoi Cell Method (VCM) based upon the treatment of the microscopic images. Comparison with the classic methods, like the Cross-Sectional Area Method and the Fibre Count Method reported in [3,4] and the conventional threshold-based Pixel Count Method, for estimation of the fibre packing factor, the proposed VCM method permits a detailed measurement at the microscopic yarn section and eliminates the errors introduced by the image boundary [2]. In [4], a quantitative way was employed to present the varied yarn sections. Typical cross-sectional shapes for warp, weft and binder yarns in a 3D woven composite were outlined by averaging the corresponding yarn contours on different slices. Polygons were used to fit the real profile of yarn.

In conventional microscopic yarn models, the sectional shape is mostly simplified as rectangular. The adopted algorithm to generate the randomly distributed fibres is normally based on Random Sequential Adsorption (RSA) method. It has difficulties to reach a higher fibre volume fraction, and even if the specified higher fibre content is reached, the computational cost would be rather huge. Such microscopic model can be found in [5]. Inspired by Ghossein's work [6], the Lubachevsky-Stillinger algorithm is adapted into 2D manner to simulate the gradient random distribution of the fibres. With such algorithm, the profile of yarn can be modelled as polygons with an arbitrary number of edges which allows an accurate reconstruction of the yarn sectional geometry. In this article, the representative yarn section is obtained from X-ray micro-tomography by averaging the outlines in different scanning slices; the IY-FVFG of the yarn is determined from micro-image observed by Scanning Electron Microscopy (SEM). The transverse yarn cracks have been investigated in [1,4,7] from microscopic observations. Similarly, the crack paths under uniaxial tensile loading have been identified during current simulations.

2 Material Investigation

2.1 Manufacturing of the composite

The preform of the fabric is made of Owen Corning® SE 1200 Type 30 E-glass roving. The preform has the thickness 1.5 mm and the areal density 1732 g/m². The ends/picks count is 6.89/6.92 yarns/cm. Vacuum infusion technique was employed to impregnate the 3D plain interlock preforms. Epolam 5015 epoxy and 5015 hardener (Axson Technology®) were mixed with mass ratio 10:3 for resin preparation. The injection was driven by -0.9 bar pressure and followed by a curing process in an autoclave at 50°C for 2 hours until the complete polymerization of the resin.

2.2 Measurements and observations

Allowing the reconstruction from high-resolution 3D images without destructing the observed sample, X-ray micro-tomography technique shows a great potential to inspect and visualise the real bulk geometry. In this work, a 3D plain interlock composite sample with rough size 4 × 3 × 2 mm³ is cut

from the impregnated panel and inspected by micro-CT scan. The acquisition of images was accomplished by Ultratom RxSolution© 3D CT system. In the current case, the nano-focus tube was chosen to produce X-rays at a working voltage of 60 kV and a working current of 70 μ A without using any additional filter. Flat panel detector of 1920×1536 pixels was utilised as an imager and the achieved resolution of the image was $4.07 \mu\text{m}/\text{pixel}$. By stacking the generated 2D slice images, the 3D volume of the examined sample was rebuilt via Avizo[®] as shown in Figure 1.

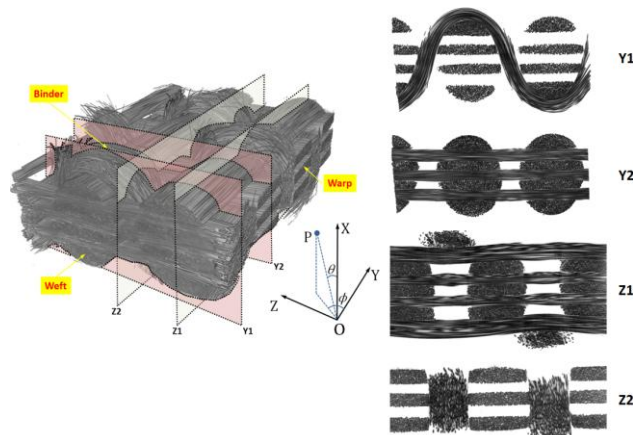


Figure 1: The reconstructed 3D volume of the inspected sample (with matrix hidden) and four representative cross-sections along warp and weft directions.

During weaving and infusion process the shapes of the yarns are varying. The measurements in the weft directions are shown in Figure 2 for example. Eight-vertex-polygon is formed to fit the real section of the middle layer yarns (i.e. the second and third layer in the weft column) by connecting the chosen feature points clockwise, while six points are selected to outline the half-lenticular sectional shapes of the outer layer yarns (i.e. the first and fourth layer in the weft column). The selection of the feature points should satisfy the following conditions: (1) a kick point on the yarn boundary is preferred, if no such point exists apparently, the midpoint of the edge would be adopted; (2) the newly determined point should help to form a convex polygon to fit the yarn profile and (3) the formed polygon should encompass fibres as many as possible.

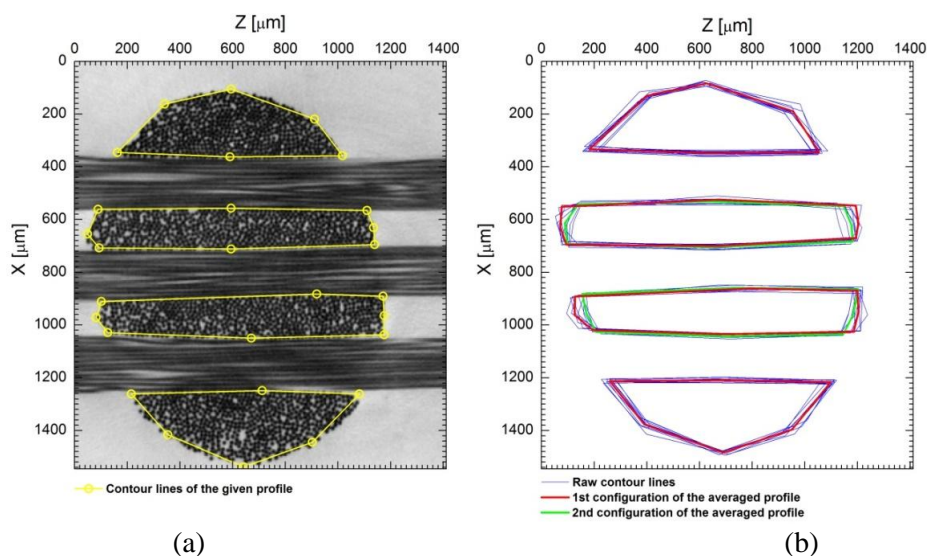


Figure 2: Measurement of the weft yarn cross sections: (a) an example scheme about choosing the feature points; (b) the averaged characteristic cross sections of weft yarn.

Remarkably, the profiles shift somehow with respect to the original positions hence each section was moved to a new averaged position so that the dimensions and shapes can be compared more easily. This explains the slight coordinates difference appeared between the real (Figure 2a) and the extracted (Figure 2b) yarn section. Outer-layer sections are roughly in half-lenticular shape, which is formed by the binding of the Z-yarn (a yarn which runs in the third/thickness direction of a fabric), and the patterns seem to vary little along the longitudinal direction. As middle layers, due to the fact that the sections shift along the running direction, two typical configurations (plotted with red and green thick lines in Figure 2b) are outlined for each layer to reflect the real situation.

Weft yarn close to the middle surface of the composite was studied in this article. In order to measure the gradient distribution of fibres, SEM images (Figure 3) were captured at 340× magnification so that the boundaries between fibre-fibre and fibre-matrix can be distinguished. 14 horizontal (in orange) and 6 vertical (in blue) movable rectangular windows are defined to calculate the fibre packing factors along the yarn width and thickness directions, as shown in the left top subplot of Figure 3.

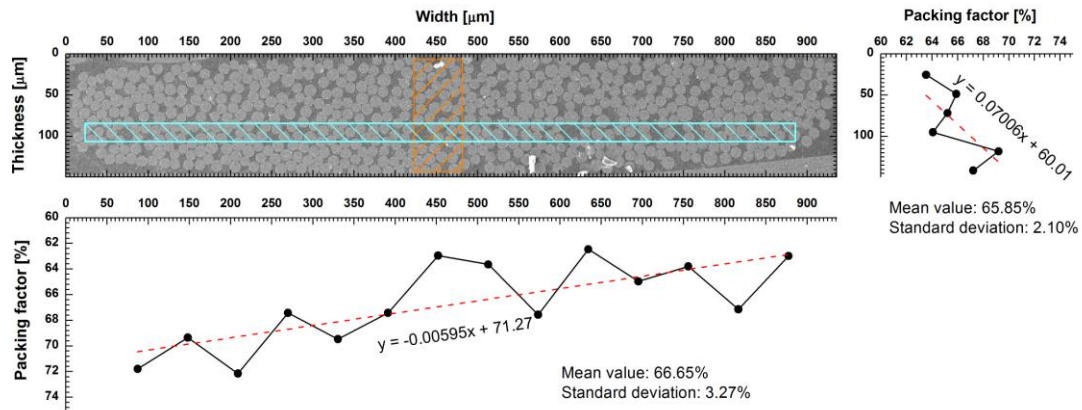


Figure 3: A representative IY-FVFG of the weft yarn along with thickness and width directions.

Binarization of the original image makes the fibre components (black pixels in this case) outstanding from the background (i.e. the matrix phase in white pixels). The median filter was then implemented onto the image to reduce the noise followed by removing the residual visible spots in the matrix-rich region. The watershed algorithm was thereafter employed to cut the connected fibre regions into individual particles. Based on the processed image, circular fibre ends were detected by Hough Circle Transform (HCT) algorithm. The coordinate of the centre point and the corresponding diameter $d_{f,i}$ are the outputs associated with each circle. The whole process was carried out by ImageJ[®].

The intra-yarn fibre volume fraction is then estimated by Eq. (1), where the S_{image} is the total area of the movable window. Only the fibres with a visible part higher than half are taken into account to calculate the effective filament number N_f .

$$V_{f,Y} = \frac{\sum_{i=1}^{N_f} \pi \cdot d_{f,i}^2}{4S_{\text{image}}} \quad (1)$$

The IY-FVFG measurement results are shown in the subplots on the left bottom and right top of Figure 3. The mean values of the packing factors measured along two directions were close. A Linear function was used to fit the scattered data. Along the yarn width direction, the fibre packing tends to be increasingly sparse from the left end to the right. The IY-FVFG is more pronounced along the yarn thickness direction than along the width.

3 Description of algorithm

The algorithm is developed on the Python platform. The real fibre shapes inside the yarn section are modelled as circles. The input data are: 1) target fibre radius r , 2) the coordinates of the outer/inner boundary points \mathbf{P}_{bdr} , 3) the target overall fibre volume fraction p_f , 4) the sub-regions and the corresponding specified fibre content p_i , 5) the rigid/flexible edges in form of coordinates and 6) maximum increment number. The main algorithm to create the yarn profile with random fibres is shown below.

Main algorithm

- 1: Input the required parameters including fibre radius (r), outer/inner boundary point coordinates (\mathbf{P}_{bdr}), target packing factor of fibre (p_f), rigid edges, flexible edges, sub-regions in quadrangle shape etc.
- 2: Generate the outer boundary of the section with shape function interpolation method
- 3: Scatter the seeds inside sub-regions
- 4: Merge the sub-regions into an entire region
- 5: **for** seed i in seed list **do**
- 6: Assign a random velocity \mathbf{v}_i
- 7: Assign a random radius growth ratio g_i
- 8: **end for**
- 9: Initialize the time $t_0 = 0$ and the actual pf at t_0 i.e. $p_0 = 0$
- 10: **while** $p_n < p_f$ **do**
- 11: Calculate the collision time of two circles t_{cls}
- 12: Calculate the collision time of the circle to the rigid edge t_{rgd}
- 13: Calculate the collision time of the circle to the flexible edge t_{flb}
- 14: $\Delta t = \min(t_{\text{cls}}, t_{\text{rgd}}, t_{\text{flb}})$
- 15: **for** each seed i in seed list **do**
- 16: Update the position from \mathbf{P}_i^n to \mathbf{P}_i^{n+1} : $\mathbf{P}_i^{n+1} = \mathbf{P}_i^n + \mathbf{v}_i^n \cdot \Delta t$
- 17: Update the radius from r_i^n to r_i^{n+1} : $r_i^{n+1} = r_i^n + g_i \cdot \Delta t \cdot \alpha^*$
- 18: **end for**
- 19: **if** $\Delta t = t_{\text{cls}}$ **do**
- 20: Exchange the collision velocity for the two seeds
- 21: **else if** $\Delta t = t_{\text{rgd}}$ **do**
- 22: Update the velocity of the seed
- 23: **else if** $\Delta t = t_{\text{flb}}$ **do**
- 24: Update the velocity of the seed
- 25: **end if**
- 26: Update p_n to p_{n+1}
- 27: **end while**
- 28: Scale the p_n to the target value p_f
- 29: Output final data list for each seed including number, coordinates and radius as well as the inner/outer vertex

* α ranges from 0 to 1.0 and is used to control the distance between two fibres. When α equals to 1.0 two fibres can be externally tangent.

The principle of the algorithm can be summarised as follow: the yarn section is discretized into several convex quadrangle sub-regions (the number depends on the user's input), the required fibre (circle) number inside each sub-region is thus determined by the local fibre volume fraction p_i and the encompassed area S_i of the sub-region. Then the random position of the circle centre, names as a seed point, is generated inside the sub-region via shape function interpolation method. The rigid edges prevent the circles from exceeding while the flexible edges permit the circles partly (less than 50%, can be specified by the user) exceed. By now the initial step is accomplished; all the generated seeds are assigned with initial random velocity and constant growth rate.

As soon as the seeds start the motion and growth, three collision times: the collision time between two

circles t_{cls} (the calculation can be referred in [6]), the collision time between the circle and rigid/flexible edges, t_{rgd}/t_{flb} , are calculated within each increment. The minimum collision time Δt is taken and all the seeds move to the new positions with the current velocities and the radii increase according to respective growth rate. For the collided circles, the velocity components, parallel to the line connecting their centres, change their directions after update of positions while the perpendicular components are kept unchanged. Once the circle is about to collide a rigid/flexible edge potentially, the velocity component perpendicular to the edge is reversed. For the magnitudes of the updated velocities discussed above, the influence of the fibre growth had been taken into account. Thereafter the obtained fibre content p_f is recalculated. The loop continues until to the specified fibre volume fraction p_f or the maximum increment number is reached.

At last, the fibre radii are rescaled to obtain an exactly specified p_f . The data list which contains the number, the coordinates, the velocities and the final radius associated with each seed are generated as output. The highest fibre packing factor that the proposed algorithm can reach is higher than 75.7% while for most 2D circular RSA the upper boundary is about 55% [8].

4 Results

Figure 4 shows the generation, motion and growth process of the seeds inside a square rigid boundary, the target fibre volume fraction is 50% and the target radius is set as 0.8 unit-length. The blue solid lines indicate the rigid boundaries while the red dash lines depict the flexible edges. The arrows, originating from the seed points, show the magnitudes and directions of the current velocity. The minimum distance between two circles are controlled more than 1.20 times (r_i+r_j) , i, j represent different circles. With such controlling, the distorted finite element can be alleviated for meshing the region where the fibres are packed more densely can be partly avoided.

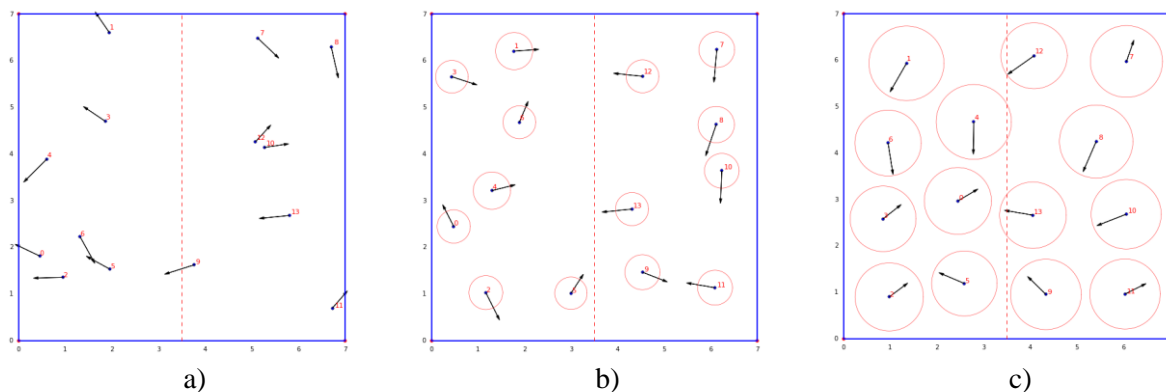


Figure 4: Test case of the square unit cell generation with target fibre packing of 50%: a) initial state; b) intermediate state and c) final state.

The generated data list is converted into a readable format for ABAQUS via Python script. Taking the final state result shown in Figure 4c as an example, the 3D geometric model of the simulated yarn section is realised by following Figure 5. The rectangular yarn section was embedded in a homogeneous medium with elastic properties equal to averaged transversely isotropic composite. Uniaxial tensile loading was imposed onto the composite boundary along the transverse direction. The displacement, principle maximal strain, and maximal principal stress contours of this simulation are shown in Figure 6.

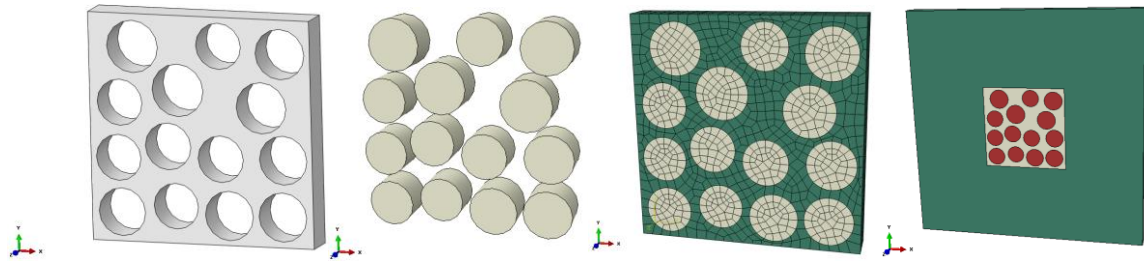


Figure 5: Geometry reconstruction in ABAQUS (targeting fibre packing is 50 %).

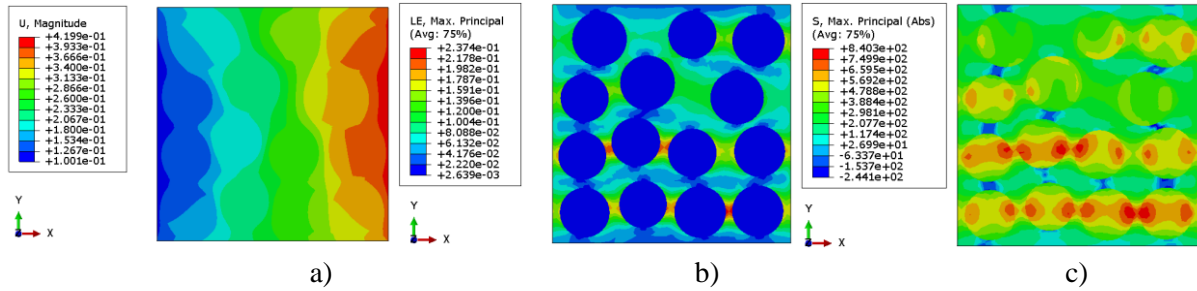


Figure 6: Elastic simulation results: a) displacement, b) principle maximal strain, and c) maximal principal stress.

Another example with more complex geometry and gradient fibre volume fractions is shown in Figure 7. The area of the yarn is divided into three sub-regions being assigned with fibre volume fractions: 50%, 60% and 70% respectively. The resultant overall packing factor is 60%. The yarn profile is simplified from the post-treated observations of the real material (Figure 2). The algorithm presents its efficiency on fitting the complex profile of yarn. For debonding simulation, the cohesive surfaces have been defined with damage criterion. Complete material data is listed in Table 1. The simulation results are shown in Figure 8. In this example, the surface-based cohesive behaviour has been incorporated. The maximum nominal stress initiation criterion and linear softening with mixed mode power law were applied. Regarding these simulation two potential sites of the transversal crack could be identified (see Figure 8a: zones with partially debonded interfaces and higher principal stresses).

Table 1: The material properties used for microscopic debonding analysis

	fiber	matrix		interface
Elastic modulus [GPa]	70	3,35	Rigidity modulus [GPa/mm]	10
Poisson's ratio	0,2	0,37	Traction strength [MPa]	30
			Fracture energy [J/m ²]	1

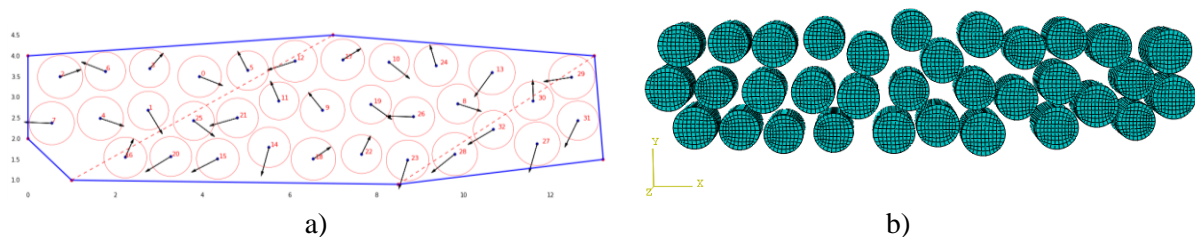


Figure 7: Test case of the irregular yarn geometry with three sub-regions of different assigned fibre volume fractions: 50%, 60% and 70%: a) final step of the algorithm and b) 3d hexagonal mesh.

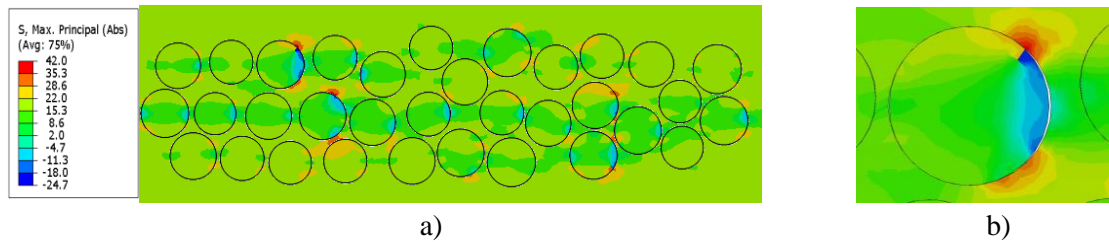


Figure 8: Results of irregular yarn shape simulation with varying fibre volume fraction: a) maximal principle stress and b) zoom to a single fibre with debonded interface.

5 Conclusions

The representative yarn sections were generated by connecting the averaged coordinates of the chosen feature points and they matched well with the real section which can be observed on each slice of 3D micro-CT results. The IY-FVFG of the real yarn is determined via an improved Fibre Count Method from the SEM images where the fibre packing factor can be measured with the horizontally/vertically movable windows.

A molecular dynamic based algorithm, which is used to simulate the gradient distribution of the fibre within the irregular yarn profile, is developed on the Python platform. The performance of the proposed algorithm is validated by models with different complexity. Compared the conventional RSA methods, it reaches a maximum fibre packing factor more than 75.7 with saving considerable computational cost.

Two numerical examples have been implemented for showing the range of possible applications of the developed algorithm. For the second example, cohesive surface behaviour has been applied in order to model fibre/matrix decohesion and detection of the transversal crack locations. The FE model of the irregular yarn shows the influence of fibre packing density on the damage zones inside the yarn.

Acknowledgement

One of the authors, Yang LIU, wishes to acknowledge sincerely the financial support of the China Scholarship Council such that this research can be undertaken. The Nord-Pas-de-Calais Region and the European Community (FEDER funds) partly funds the X-ray tomography equipment. Part of the presented results was achieved within the project JOINing of copper to aluminium by ElectroMagnetic fields – “JOIN’EM” which is funded by the European Union within the frame of the Horizon 2020 research and innovation program under Grant Agreement No. 677660.

References

- [1] Faes JC, Rezaei A, Van Paepegem W, Degrieck J. Accuracy of 2D FE models for prediction of crack initiation in nested textile composites with inhomogeneous intra-yarn fiber volume fractions. *Compos Struct* 2016;140:11–20. doi:10.1016/j.compstruct.2015.12.024.
- [2] Mühlstädt M, Seifert W, Maenz S, Jandt KD, Bossert J. Modeling of through-thickness intra-yarn volume fraction gradients in laminated woven fabrics. *ECCM17 - 17th Eur. Conf. Compos. Mater., Munich: 2016.*

- [3] Karahan M, Lomov S V., Bogdanovich AE, Mungalov D, Verpoest I. Internal geometry evaluation of non-crimp 3D orthogonal woven carbon fabric composite. *Compos Part A Appl Sci Manuf* 2010;41:1301–11. doi:10.1016/j.compositesa.2010.05.014.
- [4] Karahan M. The effect of fibre volume fraction on damage initiation and propagation of woven carbon-epoxy multi-layer composites. *Text Res J* 2011;82:45–61. doi:10.1177/0040517511416282.
- [5] Lu Z, Zhou Y, Yang Z, Liu Q. Multi-scale finite element analysis of 2.5D woven fabric composites under on-axis and off-axis tension. *Comput Mater Sci* 2013:485–94.
- [6] Ghossein E, Lévesque M. A fully automated numerical tool for a comprehensive validation of homogenization models and its application to spherical particles reinforced composites. *Int J Solids Struct* 2012;49:1387–98. doi:10.1016/j.ijsolstr.2012.02.021.
- [7] Bogdanovich AE, Karahan M, Lomov S V., Verpoest I. Quasi-static tensile behavior and damage of carbon/epoxy composite reinforced with 3D non-crimp orthogonal woven fabric. *Mech Mater* 2013;62:14–31. doi:10.1016/j.mechmat.2013.03.005.
- [8] Cadilhe A, Araújo NAM, Privman V. Random sequential adsorption: from continuum to lattice and pre-patterned substrates. *J Phys Condens Matter* 2007;19:65124. doi:10.1088/0953-8984/19/6/065124.